THE JOURNAL OF PHYSICAL CHEMISTRY C
A JOURNAL OF THE AMERICAN CHEMICAL SOCIETY

pubs.acs.org/JPCC
Article

Magnesium Adsorption on Vaterite: Influence on Dissolution Kinetics and Inhibition of the Rate of Conversion to Calcite

Morgan P. Milner, Jake M. Yang, and Richard G. Compton*

Cite This: J. Phys. Chem. C 2025, 129, 22334−22341
Read Online

ACCESS | Metrics & More | Article Recommendations | Supporting Information

ABSTRACT: We report first the influence of magnesium(II) adsorption on the dissolution kinetics of spherulitic vaterite particles. Using an inverted optical microscopy setup, the reduction in particle area in varying magnesium concentrations was tracked over time to reveal a "thermodynamically" controlled rate of dissolution. The rate was therefore controlled by both the solubility product of vaterite and the rate of diffusion of the dissolved ions away from the particle-solution surface. The variation in dissolution rate with magnesium concentration at constant ionic strength was investigated. At high magnesium concentrations, vaterite dissolution was only partially inhibited, suggesting that dissolution proceeds through at least two parallel pathways. The rate transition observed at low magnesium concentrations was fitted using a model based on Langmuirian adsorption of Mg(II). The influence of magnesium on the rate of transformation of vaterite into calcite was then investigated by aging synthesized vaterite particles in either water or a magnesium-containing solution for varying durations in the range 0 to 7 days. Scanning electron microscopy images, supported by X-ray diffraction (XRD) diffractograms, showed that the vaterite-calcite transformation was effectively inhibited by magnesium(II) concentrations of 100 mM. This suggests that seawater concentrations of magnesium suppressed calcite growth rather than reducing vaterite dissolution since the latter was measured to proceed at a significant rate in the presence of the equivalent amount of Mg(II).

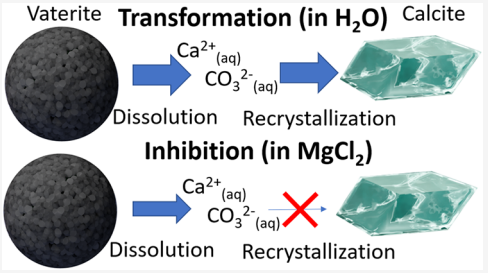

INTRODUCTION

Calcium carbonate ($CaCO_3$) is an abundant inorganic mineral found widely across both geological and biological systems. It occurs naturally in sedimentary rocks,[1] plays structural and protective roles in various organisms,[2,3] and can be synthesized by certain bacteria.[4] $CaCO_3$ exhibits three crystalline polymorphs—hexagonal vaterite, orthorhombic aragonite, and rhombohedral calcite—ranked by increasing thermodynamic stability.[5] The hydrated phases of $CaCO_3$ include monohydrocalcite, ikaite, and the recently identified hemihydrate.[6,7] Recent studies have also revealed a diverse array of amorphous calcium carbonate (ACC) states. Understanding this polyamorphism has provided valuable insights into the evolution of polymorphism, particularly in the contexts of biomineralization and controlled crystallization.[8]

Despite being metastable, vaterite occurs in nature and holds particular importance in geochemistry. It has been observed to precipitate under the distinctive sulfur-rich supraglacial conditions of a mineral spring in the Canadian High Arctic.[9] It is also found in certain mollusks, various sedimentary and rock deposits, and in the eggshells of several bird species.[10−13] Geologically, the role of $CaCO_3$ in the carbon cycle may offer valuable insights into atmospheric CO_2 levels.[14] Since the ocean absorbs approximately 30% of anthropogenic CO_2, there is a growing need to understand the crystallization and dissolution behavior of calcium carbonate under magnesium concentrations relevant to the ocean.[1,15] Although calcite, as the most stable form, has received the most study of the $CaCO_3$ polymorphs, vaterite often acts as an intermediate in its crystallization, making the fundamental study of vaterite dissolution and precipitation kinetics highly relevant in this context.[16,17]

Notably, the specific physical and chemical properties of vaterite—combined with its low production cost, and low toxicity—have expanded its use beyond traditional $CaCO_3$ applications in plastics and building materials to a wide range of biomedical fields.[18−20] Specifically, its characteristic porosity and high internal surface area enable it to incorporate significant levels of various bioactive substances, making it particularly suitable for drug delivery.[21] The enhanced dissolution rate of vaterite in acidic environments provides a mechanism for targeted chemotherapeutic delivery, allowing for penetration into tumors followed by release of the payload in the relatively more acidic extracellular environment around tumor cells.[21−23]

The growing applications and related research on vaterite have been facilitated by improved understanding of $CaCO_3$ growth mechanisms and the development of controlled synthesis methods.[10] The precipitation mechanism of $CaCO_3$, from highly supersaturated solutions of Ca^{2+} and CO_3^{2-}, is

Received: July 18, 2025
Revised: November 14, 2025
Accepted: November 25, 2025
Published: December 9, 2025

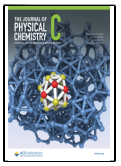

https://doi.org/10.1021/acs.jpcc.5c05009
J. Phys. Chem. C 2025, 129, 22334−22341

typically described as involving three main stages. First, amorphous calcium carbonate (ACC) nucleates. This is followed by the dissolution of the unstable ACC and its recrystallization into various polymorphs of $CaCO_3$, depending on factors such as fluid composition and temperature. In most cases, at low temperatures (<30 °C), the initial crystalline phases are vaterite and calcite. Finally, over time, the metastable vaterite dissolves and transforms into calcite, the most thermodynamically stable crystalline form of $CaCO_3$.[24−26] This is understood in terms of the Ostwald step rule, which states that the most thermodynamically stable phase is formed through intermediate metastable phases.[27−29] Due to the metastability of vaterite, a variety of additives such as organic additives, including alcohols, amino acids, and polypeptides have been explored to promote its formation during crystal growth.[30−32] These additives may also inhibit its transformation into the more thermodynamically stable calcite polymorph, both during synthesis and in later applications. Stabilization of the vaterite polymorph is often attributed to the formation of an adsorption layer on newly formed crystals during early stage precipitation. In addition, ionic cofactors such as ammonium, sulfate, and magnesium ions have been shown to stabilize vaterite when incorporated into the synthesis. Depending on the specific conditions and additives used, this stabilization is typically ascribed to the suppression of vaterite dissolution, the inhibition of calcite growth, or a combination of both.[33−36]

Fundamental study of the crystallization and dissolution of vaterite is essential for understanding its role in natural systems, optimizing its synthesis, and evaluating its effectiveness in subsequent applications. Recent advances have utilized an optical microscopy setup to study the dissolution of individual lab-grown vaterite and calcite particles, and biomineralized coccolith and coccolithophore single entities.[37−41] This method enables investigation within a well-defined, diffusive mass transport regime, overcoming the limitations of traditional techniques for studying dissolution rates, such as atomic force microscopy that either monitors the release of materials via the rate of recession of a surface or via mass loss measurements by attaching a single particle onto a cantilever.[42,43] It has been demonstrated that the dissolution of spherulitic monomer and aggregated vaterite particles proceeds under "thermodynamic control" at a rate governed by the solubility product and diffusion (rather than surface kinetic control), with aggregation affecting the time scale of dissolution but not the dissolution rate.[37,38,44] These findings highlight the importance of particle concentration, accurate modeling of solution composition, and knowledge of the aggregation state in understanding particle dissolution. A synthesis of uniform vaterite/hydroxyapatite core−shell particles has also been developed. Dissolution of these particles occurs in two thermodynamically controlled stages, an initial slower shell dissolution followed by core dissolution at the rate of pure vaterite, emphasizing the impact of surface modification on dissolution kinetics.[45]

In this work, we investigate the influence of magnesium(II) adsorption on the dissolution kinetics and phase stability of solid vaterite particles. Using optical microscopy, we show that dissolution remains thermodynamically controlled, with the rate decreasing as magnesium concentration increases. Additionally, we demonstrate that magnesium effectively inhibits the transformation of vaterite to calcite, likely by suppressing calcite growth rather than fully inhibiting the dissolution of vaterite.

EXPERIMENTAL SECTION

Materials. Ultrapurified deionized (DI) water with a resistivity no less than 18.2 MΩ·cm at 298 K and pH ≈ 6.7 (measured using a Hanna Instruments HI5221 pH meter with a HI1131B glass refillable probe) was used throughout all experiments (Milli-Q system). $CaCl_2{\cdot}2H_2O$ (≥99%) was obtained from Sigma-Aldrich, $MgCl_2{\cdot}6H_2O$ (99.999%) and NaCl (99.5%) from Thermo Fisher Scientific, and Na_2CO_3 (99.6%) was sourced from Acros Organics.

Particle Synthesis. $CaCO_3$ (vaterite) particles were synthesized following the method described by Milner et al.[37,38] Briefly, 3 mL of 1 M Na_2CO_3 solution, 9 mL of deionized water, and 3 mL of 1 M $CaCl_2{\cdot}2H_2O$ solution were combined and stirred at 650 rpm for 45 seconds. The resulting mixture was then allowed to stand undisturbed in a 25 °C water bath for 15 minutes. The particles were collected by centrifugation at 2500*g* for 1 min, resuspended in 15 mL of deionized water, and centrifuged again. Finally, the particles were suspended in 1−2 mL of methanol and air-dried at room temperature.

Dissolution Experiments. Dissolution experiments were performed using an inverted optical microscopy setup, designed for continuous monitoring of the projection area of individual particles. Details of the experimental setup, and its advantages, are discussed in Milner et al.[37,38] Synthesized $CaCO_3$ particles were suspended at a concentration of 4 $\mu g\,mL^{-1}$ in varying concentrations of $MgCl_2$, ranging from 0 to 100 mM, while maintaining a constant ionic strength of 300 mM using NaCl. The suspensions were introduced into a custom-fabricated aluminum observation chamber, and once some particles had settled on the chamber's bottom surface (within approximately 10 s), time-lapse image acquisition was initiated at 10 s intervals. Imaging was conducted under a 20× objective lens (Olympus UPLXAPO 20×, Olympus Corporation, Tokyo, Japan), with illumination provided by an LED phase-contrast light source (Aura Pro, Cairn Research, Kent, U.K.). Images were captured using an ORCA-Flash 4.0 digital camera (C13440−20CU, Hamamatsu Photonics, Japan). All experiments were conducted under ambient conditions (20 ± 2 °C).

The pH of a typical solution before dissolution is in the range 6.3 to 6.7 (pH readings throughout measured using a Hanna Instruments HI5221 pH meter with a HI1131B glass refillable probe). There is no observable change on the time scale of dissolution.

Investigation of Particle Stability and the Vaterite to Calcite Phase Transition. To investigate the effect of Mg(II) on the transformation of vaterite to calcite, 50 mg of synthesized vaterite particles were suspended in either 10 mL of deionized water or 100 mM $MgCl_2$ and kept in suspension using a fixed-speed tube rotator for varying durations. Specifically, after suspension for 1, 2, 3, 5, and 7 days, the suspensions were centrifuged at 2500*g* for 1 min, resuspended in 15 mL of deionized water, and centrifuged again. The resulting pellets were then resuspended in 1−2 mL of methanol and air-dried at room temperature.

On the addition of 5 mg/mL vaterite to 100 mM $MgCl_2$, the pH changes from 6.7 to 9.8 reflecting partial dissolution of the carbonate. The pH of a 5 mg/mL vaterite suspension in deionized (DI) water is 10.4.

For scanning electron microscopy (SEM) analysis of both these particles and untreated synthesized vaterite particles, the pertinent dried $CaCO_3$ samples were dispersed onto carbon tape affixed to aluminum stubs. The samples were then sputter-

https://doi.org/10.1021/acs.jpcc.5c05009
J. Phys. Chem. C 2025, 129, 22334−22341

coated with nanometer thicknesses of gold and analyzed using a Zeiss Sigma 300 FEG-SEM instrument operating at an accelerating voltage of 2 kV. Images were acquired at different magnifications, with magnification defined as the ratio of the image field length to the actual scan length.

X-ray diffraction patterns of unmodified particles, as well as those suspended in deionized water or 100 mM $MgCl_2$ for 3 and 7 days, were obtained using a Bruker D8 Advance Eco X-ray powder diffractometer with Cu Kα1,2 radiation. The XRD pattern was collected with a 2θ range of 15 to 60° in increments of 0.031° and a scan time of 0.74 s per step.

Data Analysis. Images obtained from the optical microscopy setup were analyzed using the ImageJ freeware package (Fiji). For the dissolution experiments, the projected area of each particle (in pixels) was determined using the "Default" autothresholding algorithm in ImageJ. The latter generates a binary image where white pixels represent the particle projections and black pixels denote the background. The choice of thresholding method is supported by previous publications.[44] The pixel count corresponding to each particle was then converted to actual projected area using the known pixel-to-distance ratio. ImageJ was also employed for analysis and editing of SEM images. Graphical plotting and data fitting for the dissolution results, as well as plotting of the XRD data, was carried out using OriginPro 2023.

RESULTS AND DISCUSSION

In the following, we first report the effect of Mg^{2+} on the dissolution behavior of single, unaggregated vaterite particles across a concentration range of 0 to 100 mM $MgCl_2$, at constant total ionic strength, to distinguish between kinetic and thermodynamic control. A decrease in dissolution rate as a function of increasing Mg^{2+} is seen. This is attributed to Mg^{2+} adsorption and is shown to be in quantitative agreement with the Langmuiran adsorption isotherm. Second, the interconversion of vaterite particles to calcite, when suspended in aqueous media, was investigated using scanning electron microscopy and X-ray diffraction. Mg^{2+} is shown to be an effective inhibitor compared to the transformation as observed in deionized water.

Magnesium(II) Adsorption and Vaterite Dissolution Kinetics. The dissolution kinetics of synthesized vaterite particles were studied in 10 mL aqueous solutions containing varying concentrations of Mg^{2+} (0−100 mM), with the total ionic strength maintained at 300 mM using NaCl. A particle concentration of 4 μg mL^{-1} was used to minimize diffusional overlap between neighboring particles, a factor previously shown to reduce apparent dissolution rates; at this concentration the effect is negligible, indicating an acceptable limit for reliable measurements.[37,38] At the start of all dissolution experiments, the particle suspension was introduced into the observation chamber, and approximately 10 s were allowed for a small number of particles to settle on the bottom surface; the focus was then optimized for imaging. Time-lapse images were recorded at regular intervals using the inverted optical microscopy setup, and the reduction in particle size was quantified by extracting the projected area of nonagglomerated spherical particles as a function of time, as detailed in the Experimental Section. Plots of area versus time for particles studied at 0 mM and 100 mM Mg^{2+} are presented in Figure 1, where the data have been shifted along the x-axis to collectively represent the dissolution trend for particles with different initial sizes. At all magnesium(II) concentrations studied, and for multiple particles (n = 5 per condition), a constant rate of area

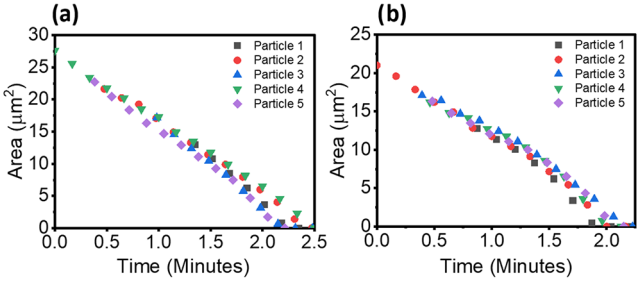

Figure 1. Measured projection areas of five individual vaterite particles plotted as a function of time during dissolution in solutions containing (a) 0 mM and (b) 100 mM Mg^{2+}, with the overall ionic strength maintained at 300 mM using NaCl. The time axes for each particle were shifted to collectively illustrate the dissolution trend across particles with different initial sizes.

reduction over time was observed within experimental error. A nonlinear variation in particle diameter with time follows directly from the observed linear variation in particle area with time. The overall trend of linear dA/dt is clear across the full dissolution time scale, especially when contrasted with the pronounced nonlinearity of the plots of dL/dt. The Supporting Information provides plots of both area and diameter versus time for all particles at each Mg^{2+} concentration studied—namely 0, 2.5, 5, 10, 20, 30, 40, 55, 70, 85, and 100 mM.

In accordance with previous studies, two limiting cases can be recognized for the dissolution of a particle on a surface, where the overall rate is generally an interplay between interfacial kinetics and mass transport.[37,38,44] Under thermodynamic control, slow and rate-limiting mass transport causes the dissolution rate to depend on both the solubility product of the solid and the diffusion coefficients of the dissolved species. In contrast, under kinetic control, relatively rapid mass transport means that the rate is determined solely by the interfacial reaction kinetics. For the specific case of $CaCO_3$ dissolution, this is illustrated by eqs 1 and 2, representing thermodynamic and kinetic control, respectively.

$$CaCO_3(s) \underset{k_b}{\overset{k_f}{\rightleftharpoons}} Ca^{2+}(aq) + CO_3^{2-}(aq) \xrightarrow{k_{mt}} \text{bulk} \quad (1)$$

$$CaCO_3(s) \xrightarrow{k_{ir}} Ca^{2+}(aq) + CO_3^{2-}(aq) \quad (2)$$

Note that under the assumption of rate limiting Fickian diffusion, a spherical particle resting on a surface at steady state is surrounded by a saturated layer of dissolved material. The diffusion rate is similar to that of an isolated particle but reduced by a numerical factor, however, the dependence on particle size, diffusion coefficient, and other parameters remains unchanged. In this geometry, the diffusion field at steady-state is approximately hemispherical.[46,47] Based on these observations, and as derived by Milner et al.[37,38] for spherulitic vaterite particles, kinetic control is characterized by a constant rate of change in particle radius (dr/dt) and a nonconstant change in projected area (dA/dt), whereas thermodynamic control results in a size-dependent dr/dt and a constant dA/dt. Hence, the linearity of the area-versus-time plots in Figure 1 indicates that dissolution in the presence of adsorption also proceeds under thermodynamic control for vaterite particles at all Mg^{2+} concentrations, as it does for both monomeric and aggregated pure vaterite particles in deionized water.[37,38,44] Further

https://doi.org/10.1021/acs.jpcc.5c05009
J. Phys. Chem. C 2025, 129, 22334−22341

background and discussion of the dissolution model are provided in the Supporting Information. Note that the pH of a typical solution prior to dissolution is in the range of 6.3 to 6.7, and it remains constant over the time scale of dissolution. If the process were proton-driven, this would manifest as a deviation from linearity in the area-versus-time plot, since, under thermodynamic control, the rate is governed by the diffusion of material away from the solid.

By applying a linear fit to the region corresponding to the first 50% reduction in projected area, an average dissolution rate for each Mg^{2+} concentration was determined, as shown in Figure 2.

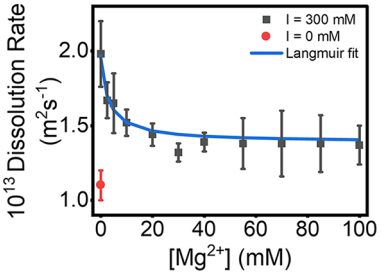

Figure 2. Average dissolution rate as a function of Mg^{2+} concentration, with the overall ionic strength of the solution maintained at 300 mM using NaCl. For 0 mM Mg^{2+}, the average dissolution rate at 0 mM ionic strength (i.e., in deionized water), as reported by Milner et al., is also included, with the ionic strength indicated in the figure legend.[37,38] Rates were determined from area−time plots for five particles per concentration, using the slope corresponding to the region in which the particle area decreased to 50% of its initial value. The average dissolution rate was calculated from these individual slopes, with error bars representing the variance among the data (n = 5). The blue line represents the Langmuir fit of the data according to the model described in eqs 3−6.

Note that only the first 50% reduction in projection area is used for fitting, in order to focus on the data best resolved by the camera's resolution. This corresponds to when the particle is larger and therefore closest in size to the range for which focus was optimized, as the focus is not adjusted in vertical height as particles dissolve. The average dissolution rate in the absence of Mg^{2+}, but with ionic strength maintained at 300 mM using NaCl, is approximately $2.0 \pm 0.2 \times 10^{-13}$ m^2 s^{-1}, in contrast to the previously reported rate of $1.1 \pm 0.1 \times 10^{-13}$ m^2 s^{-1} for monomeric vaterite particles at the same particle concentration but in pure deionized water.[37,38] This increase is attributed to increasing ionic strength increasing the rate of dissolution. A similar effect has been reported for the dissolution of calcite.[48] At the same time, for increasing concentrations of Mg^{2+} at constant ionic strength, a clear trend of decreasing dissolution rate is observed; specifically, the rate decreases from $\sim 2.0 \pm 0.2 \times 10^{-13}$ m^2 s^{-1} at 0 mM Mg^{2+} (300 mM NaCl) to $1.4 \pm 0.1 \times 10^{-13}$ m^2 s^{-1} at 100 mM Mg^{2+}. Note that the solution containing 300 mM of NaCl and 0 mM of Mg^{2+} has the same ionic strength as the solution containing only 100 mM Mg^{2+}. Moreover, by maintaining a constant ionic strength with the use of NaCl an inert electrolyte, a marked decrease in dissolution rate is observed as the Mg^{2+} concentration increases from 0 to 20 mM, followed by an approximate leveling off at higher concentrations up to 100 mM. The decrease in rate with increasing Mg^{2+} concentrations is attributed to the adsorption of Mg^{2+} given previous reports of magnesium adsorption on calcium carbonate materials.[49,50]

Interestingly, the rate observed at 100 mM Mg^{2+} and a high ionic strength of 300 mM is similar to, though slightly higher than, that observed in deionized water. This behavior can be attributed to the interplay of two opposing factors. First, at 0 mM Mg^{2+}, there is an increase in rate, relative to dissolution in deionized water, due to the ionic strength effect.[48] Second, as the concentration of Mg^{2+} is increased, there is a reduction in dissolution rate due to Mg^{2+} adsorption onto the particle surface, blocking the surface dissolution.[51]

At Mg^{2+} concentrations above 50−55 mM, $MgCO_3$ formation becomes thermodynamically possible, according to reported equilibrium constants.[48] However, analysis of the dissolution experiments, presented in Figure 2, show that the rate effectively plateaus above 40 mM Mg^{2+}. At this concentration, $MgCO_3$ formation is not possible. The absence of a further decrease in rate at higher concentrations therefore indicates that $MgCO_3$ formation is not a contributing factor to the observed Mg^{2+} concentration dependence of the dissolution rate. The reduction in rate up to this point can therefore be attributed to Mg^{2+} adsorption. Beyond this concentration, no decrease in rate is observed, which would not be expected if an inhibitory $MgCO_3$ layer were forming. These observations support the conclusion that the dissolution rate is primarily governed by Mg^{2+} adsorption.

Within the constraints of thermodynamically controlled dissolution, where the rate of dissolution is limited by mass transport of dissolved ions from the surface, the concentrations of dissolved ions at the particle-solution boundary are in equilibrium with the solid. The concentrations are fixed by the solubility product of the dissolving solid. This determines the amount of material available for mass transport away across the diffusion layer surrounding the particle. Together the solubility and the diffusion rate govern the overall rate of dissolution as controlled by Fick's Laws of Diffusion.[52,53] Note that the particle radius dependence of the rate of diffusion means that the molar flux J (mol m^{-2} s^{-1}) varies as dissolution proceeds and the particles shrink. This along with a detailed discussion of the dissolution model, is included in the Supporting Information. If surface adsorption of certain species occurs while thermodynamic control is maintained, and if the ion concentrations near the particle surface remain in equilibrium with the solid, these are governed by an effective solubility product and solute fluxes. Yang et al.[51] have demonstrated that under such combined thermodynamic and mass transport control, the amount of material in the diffusion layer is reduced by a factor of $1 - \theta$, where θ is the fractional surface coverage of the adsorbed inhibitor, which in the case of interest is dependent on [Mg^{2+}]. Accordingly, in our case, the presence of Mg^{2+} is expected to reduce the reaction rate - relative to its absence ($Rate_{MT}$) − by a factor of $1 - \theta$, as expressed in eq 3 where the subscript MT denotes thermodynamic/mass transport control.

$$\text{rate} = (1 - \theta)\text{rate}_{MT} \tag{3}$$

This expression permits the inference of θ at a given [Mg^{2+}] from the data from Figure 2, knowing the rate at [Mg^{2+}] = 0 mM, as shown in Figure 3a. In the simple case of Langmuirian adsorption the fractional coverage, θ, is

$$\theta = \theta_{max}\frac{K[Mg^{2+}]}{1 + K[Mg^{2+}]} \tag{4}$$

where K is the equilibrium constant for Mg^{2+} adsorption that varies with pressure and temperature, given in units of inverse

https://doi.org/10.1021/acs.jpcc.5c05009
J. Phys. Chem. C 2025, 129, 22334−22341

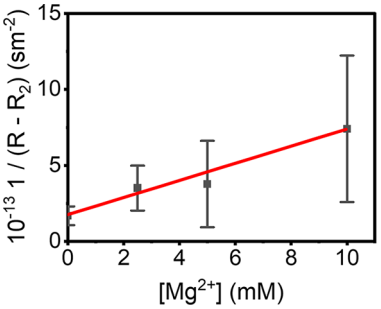

Figure 3. Plot of $1/(R - R_2)$ as a function of $[Mg^{2+}]$ in the 0−10 mM concentration range, with a linear fitting applied. The same experimental data presented in Figure 2 were used to generate these plots.

concentration, and θ_{max} is the maximum fractional coverage achieved in the studied $[Mg^{2+}]$, introduced as a normalization factor. The data is Figure 2 shows that magnesium adsorption leads to partial but not full inhibition of the dissolution even at high levels of magnesium(II). This is consistent with the idea that dissolution proceeds via at least two different parallel pathways reflecting difference surface features. Thus, the overall dissolution rate, R, can be expressed as

$$R = R_1 + R_2 \tag{5}$$

where R is the total dissolution rate, R_1 is the dissolution pathway influenced by the magnesium adsorption and R_2 reflects the pathway(s) insensitive to adsorption. From the discussion above and eq 3 we can write

$$R_1 = R_1^* \frac{1}{1 + K[Mg^{2+}]} \tag{6}$$

where R_1* is the rate of the R_1 process in the absence of magnesium. R_2 is easily estimated from the plateau region in Figure 2 noted for high magnesium concentrations. The data in Figure 2 can thus be analyzed for the Langmuir adsorption constant, K, by plotting the reciprocal of $(R - R_2)$ against $[Mg^{2+}]$ where a straight line indicates the Langmuir character of the adsorption, the intercept corresponds to $1/R_1$* and the slope to K/R_1*. Thus, combining the slope and intercept yields a value of K. Figure 3 shows the corresponding analysis and gives the values of $R_1^* = 0.58 \times 10^{-13}$ m^2 s^{-1}, $R_2 = 1.4 \times 10^{-13}$ m^2 s^{-1} and $K = 0.33$ m^3 mol^{-1}. We are unaware of any previous quantitative data for magnesium adsorption on vaterite but values for calcite of $K = 0.22$ m^3 mol^{-1} and $K = 0.23$ m^3 mol^{-1} have been reported.[49,50] Using these values, and in accordance with eqs 5 and 6, note that Figure 2 also presents a fit over the full concentration range of the experimental data based on the established model, demonstrating good agreement between the two.

Controlling Vaterite to Calcite Transformation. Next, the influence of Mg^{2+} on the transformation of vaterite to calcite was investigated by suspending synthesized vaterite particles in either deionized water or 100 mM aqueous $MgCl_2$. The particle concentration was set to 5 mg/mL to ensure that, after an initial degree of particle dissolution, the solution rapidly becomes saturated with respect to $CaCO_3$ and reaches equilibrium. Suspensions were incubated for 1, 2, 3, 5, or 7 days using a fixed-speed tube rotator to gently mix and maintain the particles in suspension. After incubation, the particles were separated, dried, and imaged using scanning electron microscopy (SEM). Note that the pH of the suspension formed after adding 5 mg of vaterite per 1 mL of 100 mM $MgCl_2$ or deionized water is 9.8 and 10.4, respectively reflecting partial dissolution of the solid. However, the changes in these solutions, including the final pH, are comparable, indicating that any observed differences must be attributed to the effect of magnesium. For reference, an SEM image of unsuspended, as synthesized vaterite particles is provided in Figure 4. Representative SEM images of particles

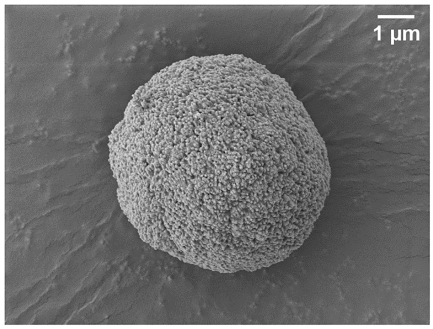

Figure 4. SEM image of synthesized vaterite particles, captured at 10,000× magnification.

following suspension for 3 and 7 days in both deionized water and 100 mM $MgCl_2$ are shown in Figures 5 and 6, respectively. SEM images for all suspension times studied, in both deionized water and 100 mM $MgCl_2$, along with images of unmodified synthesized vaterite, are provided in the Supporting Information. Before any exposure to water or $MgCl_2$, the synthesized material predominantly consists of nonagglomerated spherulitic vaterite particles that are approximately spherical in shape and composed of distinctive nanosized spherical subunits. A proportion of the sample also contains aggregated particles, including dimers and larger clusters, as well as a small amount of calcite formed during synthesis. These features are evident in the SEM images provided in the Supporting Information. As the suspension time in deionized water, saturated with respect to calcium carbonate, increases, the vaterite particles are observed to aggregate into larger clusters. Simultaneously, the appearance of smooth crystalline planes characteristic of rhombohedral calcite becomes more prominent. In images of particles suspended in deionized water for intermediate durations within the studied time range, particles exhibit both vaterite and calcite characteristics simultaneously, as shown in Figure 5a. After 7 days in deionized water, the particles displayed only the distinctive smooth surfaces characteristic of calcite (see Figure 6a). In contrast, particles suspended in 100 mM $MgCl_2$ retained the spherical morphology of vaterite at all time points studied, as evident in Figures 5b and 6b. No notable increase in the proportion of calcite relative to vaterite was observed in the SEM images.

To further examine the influence of Mg^{2+} on the transformation of vaterite to calcite, X-ray diffraction (XRD) patterns were collected for untreated particles, as well as for particles suspended in deionized water or 100 mM $MgCl_2$ for 3 and 7 days. In deionized water, the intensity of the characteristic calcite peaks increased relative to the vaterite peaks from 0 to 3 days, with vaterite peaks no longer detectable after 7 days. In contrast, for particles suspended in 100 mM $MgCl_2$, there was no significant increase in calcite peak intensity relative to vaterite after either 3 or 7 days. The diffractograms and a more detailed discussion of the XRD results are provided in the Supporting Information.

https://doi.org/10.1021/acs.jpcc.5c05009
J. Phys. Chem. C 2025, 129, 22334−22341

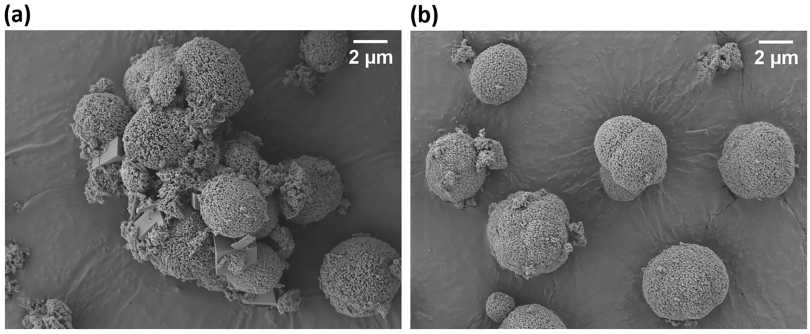

Figure 5. SEM image of particles after suspension of synthesized vaterite particles in (a) deionized water and (b) 100 mM $MgCl_2$ for 3 days. The images were captured at 5000× magnification.

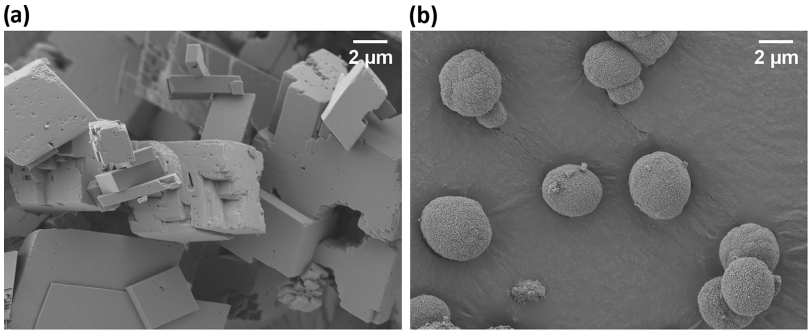

Figure 6. SEM image of particles after suspension of synthesized vaterite particles in (a) deionized water and (b) 100 mM $MgCl_2$ for 7 days. The images were captured at 5000× magnification.

The combined SEM and XRD results suggest that in deionized water, under the specific conditions studied, the transformation from vaterite to calcite for the particles studied is a gradual process that completes within 7 days. In contrast, 100 mM Mg^{2+} effectively halts this transformation, preserving the characteristic spherical and spherulitic morphology of vaterite and reducing aggregation. The processes observed in deionized water can be interpreted as two simultaneous but related phenomena: (a) Ostwald ripening of vaterite monomers and smaller aggregates into larger clusters, and (b) the transformation of vaterite into the more thermodynamically stable calcite polymorph. According to the Ostwald step rule, an energetically downhill transformation would predict a vaterite-to-calcite conversion via aragonite.[27,29] However, the aragonite polymorph is rarely observed under similar conditions (<30 °C) during calcite precipitation from aqueous solution, a phenomenon attributed to heterogeneous nucleation on the surface of vaterite.[28] The basic chemistry of the transformation of suspensions in water of vaterite into calcite can rather be understood as a two-stage process, namely the dissolution of vaterite followed by recrystallization into calcite. Hence, the inhibition of calcite formation in the presence of 100 mM $MgCl_2$ must be understood in terms of its effect on one of these processes. Dissolution experiments show that the dissolution rate in 100 mM $MgCl_2$ is similar to that in deionized water, because Mg^{2+} adsorption offsets the effect of increased ionic strength. Therefore, the suppression of the vaterite-to-calcite conversion is best explained by inhibition of calcite crystal growth. As previously reported in the context of calcite crystallization, this has been attributed to Mg^{2+} adsorption on the calcite surface, which suppresses particle growth.[34]

CONCLUSIONS

The results demonstrate that Mg(II) adsorption has a significant effect on the dissolution kinetics of solid vaterite particles. Thermodynamically controlled conditions were shown to operate with the dissolution rate governed by both the solubility product, pinning the maximum concentration of dissolved ions at the particle-solution interface, and the diffusion of ions away from the particle surface. A clear dependence on magnesium concentration was observed. At low Mg^{2+} concentrations, the variation in dissolution rate is consistent with a Langmuir-type adsorption model. The continued appreciable dissolution at high magnesium concentrations indicates that the process proceeds through at least two parallel pathways, only one of which is sensitive to magnesium adsorption. The similar dissolution rate observed in 100 mM $MgCl_2$ and pure water was attributed to the opposing influences of Mg^{2+} adsorption, which slows dissolution, and an increased ionic strength in the solution phase, which enhances it.

Mg(II) was shown to reduce the rate of vaterite to calcite transformation compared to that observed in deionized water. As dissolution of vaterite remained appreciable in the presence of Mg^{2+}, this inhibition was attributed to the suppression of calcite crystal growth rather than a decrease in vaterite dissolution.

Holistically, these findings highlight the critical role of surface-adsorbed species in governing the stability and transformation pathways of metastable calcium carbonate phases. These findings are of particular importance in understanding the longevity of natural and biomineralised vaterite crystalline materials in the marine environment, where the latter contains ca. 55 mM of Mg^{2+}.

https://doi.org/10.1021/acs.jpcc.5c05009
J. Phys. Chem. C 2025, 129, 22334−22341

■ ASSOCIATED CONTENT

Supporting Information

The Supporting Information is available free of charge at https://pubs.acs.org/doi/10.1021/acs.jpcc.5c05009.

Includes area and diameter vs time plots and corresponding raw data for the study on the influence of Mg (II) adsorption on vaterite dissolution kinetics. Further detail on the model for particle dissolution and the effect of adsorption is provided. Also provided are SEM images and XRD diffractograms related to the investigation of Mg^{2+} (aq) effects on the transformation of vaterite into calcite (PDF)

■ AUTHOR INFORMATION

Corresponding Author

Richard G. Compton − *Physical and Theoretical Chemistry Laboratory, Department of Chemistry, University of Oxford, Oxford OX1 3QZ, Great Britain;* orcid.org/0000-0001-9841-5041; Email: richard.compton@chem.ox.ac.uk

Authors

Morgan P. Milner − *Physical and Theoretical Chemistry Laboratory, Department of Chemistry, University of Oxford, Oxford OX1 3QZ, Great Britain*

Jake M. Yang − *Centre for Sustainable Materials Processing, School of Chemistry, University of Leicester, Leicester LE1 7RH, Great Britain;* orcid.org/0000-0001-8829-5883

Complete contact information is available at: https://pubs.acs.org/10.1021/acs.jpcc.5c05009

Notes

The authors declare no competing financial interest.

■ ACKNOWLEDGMENTS

This work was carried out with support from the University of Oxford.

■ REFERENCES

(1) Morse, J. W.; Arvidson, R. S.; Lüttge, A. Calcium Carbonate Formation and Dissolution. *Chem. Rev.* **2007**, *107* (2), 342−381.

(2) Kertmen, A.; Petrenko, I.; Schimpf, C.; Rafaja, D.; Petrova, O.; Sivkov, V.; Nekipelov, S.; Fursov, A.; Stelling, A. L.; Heimler, K.; et al. Calcite Nanotuned Chitinous Skeletons of Giant Ianthella Basta Marine Demosponge. *Int. J. Mol. Sci.* **2021**, *22* (22), No. 12588.

(3) Murphy, J. N.; Schneider, C. M.; Hawboldt, K.; Kerton, F. M. Hard to Soft: Biogenic Absorbent Sponge-like Material from Waste Mussel Shells. *Matter* **2020**, *3* (6), 2029−2041.

(4) Simon, P.; Pompe, W.; Gruner, D.; Sturm, E.; Ostermann, K.; Matys, S.; Vogel, M.; Rödel, G. Nested Formation of Calcium Carbonate Polymorphs in a Bacterial Surface Membrane with a Graded Nanoconfinement: An Evolutionary Strategy to Ensure Bacterial Survival. *ACS Biomater. Sci. Eng.* **2022**, *8* (2), 526−539.

(5) Liendo, F.; Arduino, M.; Deorsola, F. A.; Bensaid, S. Factors Controlling and Influencing Polymorphism, Morphology and Size of Calcium Carbonate Synthesized through the Carbonation Route: A Review. *Powder Technol.* **2022**, *398*, No. 117050.

(6) Demichelis, R.; Raiteri, P.; Gale, J. D. Structure of Hydrated Calcium Carbonates: A First-Principles Study. *J. Cryst. Growth* **2014**, *401*, 33−37.

(7) Zou, Z.; Habraken, W. J. E. M.; Matveeva, G.; Jensen, A. C. S.; Bertinetti, L.; Hood, M. A.; Sun, C.; Gilbert, P. U. P. A.; Polishchuk, I.; Pokroy, B.; et al. A Hydrated Crystalline Calcium Carbonate Phase: Calcium Carbonate Hemihydrate. *Science* **2019**, *363* (6425), 396−400.

(8) Cartwright, J. H. E.; Checa, A. G.; Gale, J. D.; Gebauer, D.; Sainz-Díaz, C. I. Calcium Carbonate Polyamorphism and Its Role in Biomineralization: How Many Amorphous Calcium Carbonates Are There? *Angew. Chem., Int. Ed.* **2012**, *51* (48), 11960−11970.

(9) Grasby, S. E. Naturally Precipitating Vaterite (μ-CaCO3) Spheres: Unusual Carbonates Formed in an Extreme Environment. *Geochim. Cosmochim. Acta* **2003**, *67* (9), 1659−1666.

(10) Konopacka-Łyskawa, D. Synthesis Methods and Favorable Conditions for Spherical Vaterite Precipitation: A Review. *Crystals* **2019**, *9* (4), No. 223.

(11) Friedman, G. M.; Schultz, D. J. Precipitation of Vaterite ($CaCO_3$) during Oil Field Drilling. *Mineral. Mag.* **1994**, *58* (392), 401−408.

(12) Portugal, S. J.; Bowen, J.; Riehl, C. A Rare Mineral, Vaterite, Acts as a Shock Absorber in the Eggshell of a Communally Nesting Bird. *Ibis* **2018**, *160* (1), 173−178.

(13) Spann, N.; Harper, E. M.; Aldridge, D. C. The Unusual Mineral Vaterite in Shells of the Freshwater Bivalve Corbicula Fluminea from the UK. *Naturwissenschaften* **2010**, *97* (8), 743−751.

(14) Ridgwell, A.; Zeebe, R. The Role of the Global Carbonate Cycle in the Regulation and Evolution of the Earth System. *Earth Planet. Sci. Lett.* **2005**, *234* (3−4), 299−315.

(15) Feely, R. A.; Sabine, C. L.; Lee, K.; Berelson, W.; Kleypas, J.; Fabry, V. J.; Millero, F. J. Impact of Anthropogenic CO_2 on the $CaCO_3$ System in the Oceans. *Science* **2004**, *305* (5682), 362−366.

(16) Lassin, A.; André, L.; Devau, N.; Lach, A.; Beuvier, T.; Gibaud, A.; Gaboreau, S.; Azaroual, M. Dynamics of Calcium Carbonate Formation: Geochemical Modeling of a Two-Step Mechanism. *Geochim. Cosmochim. Acta* **2018**, *240*, 236−254.

(17) Rodriguez-Blanco, J. D.; Sand, K. K.; Benning, L. G. ACC and Vaterite as Intermediates in the Solution-Based Crystallization of CaCO3. In *New Perspectives on Mineral Nucleation and Growth*; Springer International Publishing: Cham, 2017; pp 93−111.

(18) Trushina, D. B.; Bukreeva, T. V.; Kovalchuk, M. V.; Antipina, M. N. CaCO3 Vaterite Microparticles for Biomedical and Personal Care Applications. *Mater. Sci. Eng., C* **2014**, *45*, 644−658.

(19) Garcia, F. Changes of Surface and Volume Properties of Calcite during a Batch Wet Grinding Process. *Chem. Eng. J.* **2002**, *85* (2−3), 177−187.

(20) Saulat, H.; Cao, M.; Khan, M. M.; Khan, M.; Khan, M. M.; Rehman, A. Preparation and Applications of Calcium Carbonate Whisker with a Special Focus on Construction Materials. *Constr. Build. Mater.* **2020**, *236*, No. 117613.

(21) Trushina, D. B.; Borodina, T. N.; Belyakov, S.; Antipina, M. N. Calcium Carbonate Vaterite Particles for Drug Delivery: Advances and Challenges. *Mater. Today Adv.* **2022**, *14*, No. 100214.

(22) Yang, T.; Ao, Y.; Feng, J.; Wang, C.; Zhang, J. Biomineralization Inspired Synthesis of CaCO3-Based DDS for PH-Responsive Release of Anticancer Drug. *Mater. Today Commun.* **2021**, *27*, No. 102256.

(23) Kato, Y.; Ozawa, S.; Miyamoto, C.; Maehata, Y.; Suzuki, A.; Maeda, T.; Baba, Y. Acidic Extracellular Microenvironment and Cancer. *Cancer Cell Int.* **2013**, *13* (1), No. 89.

(24) Rodriguez-Blanco, J. D.; Shaw, S.; Benning, L. G. The Kinetics and Mechanisms of Amorphous Calcium Carbonate (ACC) Crystallization to Calcite, Viavaterite. *Nanoscale* **2011**, *3* (1), 265−271.

(25) Bots, P.; Benning, L. G.; Rodriguez-Blanco, J.-D.; Roncal-Herrero, T.; Shaw, S. Mechanistic Insights into the Crystallization of Amorphous Calcium Carbonate (ACC). *Cryst. Growth Des.* **2012**, *12* (7), 3806−3814.

(26) Ogino, T.; Suzuki, T.; Sawada, K. The Formation and Transformation Mechanism of Calcium Carbonate in Water. *Geochim. Cosmochim. Acta* **1987**, *51* (10), 2757−2767.

(27) Morse, J. W.; Casey, W. H. Ostwald Processes and Mineral Paragenesis in Sediments. *Am. J. Sci.* **1988**, *288* (6), 537−560.

(28) Myszka, B.; Schüßler, M.; Hurle, K.; Demmert, B.; Detsch, R.; Boccaccini, A. R.; Wolf, S. E. Phase-Specific Bioactivity and Altered Ostwald Ripening Pathways of Calcium Carbonate Polymorphs in Simulated Body Fluid. *RSC Adv.* **2019**, *9* (32), 18232−18244.

(29) Ostwald, W. Studien Über Die Bildung Und Umwandlung Fester Körper. *Z. Phys. Chem.* **1897**, *22U* (1), 289−330.
(30) Manoli, F.; Dalas, E. Spontaneous Precipitation of Calcium Carbonate in the Presence of Ethanol, Isopropanol and Diethylene Glycol. *J. Cryst. Growth* **2000**, *218* (2−4), 359−364.
(31) Chuajiw, W.; Takatori, K.; Igarashi, T.; Hara, H.; Fukushima, Y. The Influence of Aliphatic Amines, Diamines, and Amino Acids on the Polymorph of Calcium Carbonate Precipitated by the Introduction of Carbon Dioxide Gas into Calcium Hydroxide Aqueous Suspensions. *J. Cryst. Growth* **2014**, *386*, 119−127.
(32) Njegić-Džakula, B.; Falini, G.; Brečević, L.; Skoko, Ž.; Kralj, D. Effects of Initial Supersaturation on Spontaneous Precipitation of Calcium Carbonate in the Presence of Charged Poly-l-Amino Acids. *J. Colloid Interface Sci.* **2010**, *343* (2), 553−563.
(33) Williams, J. M.; Zhao, D.; Moon, S.; Kawashima, S.; Park, A.-H. A.; Moment, A. J. Stabilization of Pure Vaterite During Carbon Mineralization: Defining Critical Activities, Additive Concentrations, and Gas Flow Conditions for Carbon Utilization. *Cryst. Growth Des.* **2023**, *23* (11), 8103−8115.
(34) Kitamura, M. Crystallization and Transformation Mechanism of Calcium Carbonate Polymorphs and the Effect of Magnesium Ion. *J. Colloid Interface Sci.* **2001**, *236* (2), 318−327.
(35) Katsifaras, A.; Spanos, N. Effect of Inorganic Phosphate Ions on the Spontaneous Precipitation of Vaterite and on the Transformation of Vaterite to Calcite. *J. Cryst. Growth* **1999**, *204* (1−2), 183−190.
(36) Song, X.; Tang, Z.; Hua, X.; Li, M.; Chen, T.; He, P. Effects of K Ions on the Vaterite CaCO3 Formation Using the Steamed Ammonia Liquid Waste as Calcium Sources. *Powder Technol.* **2025**, *463*, No. 121172.
(37) Milner, M. P.; Yang, M.; Compton, R. G. Vaterite Dissolution: Mechanism and Kinetics. *J. Phys. Chem. C* **2024**, *128* (25), 10388−10396.
(38) Milner, M. P.; Yang, M.; Compton, R. G. Correction to Vaterite Dissolution: Mechanism and Kinetics. *J. Phys. Chem. C* **2024**, *128* (40), 17196.
(39) Fan, X.; Batchelor-McAuley, C.; Yang, M.; Compton, R. G. Single Calcite Particle Dissolution Kinetics: Revealing the Influence of Mass Transport. *ACS Meas. Sci. Au* **2022**, *2* (5), 422−429.
(40) Yang, M.; Batchelor-McAuley, C.; Barton, S.; Rickaby, R. E. M.; Bouman, H. A.; Compton, R. G. Calcifying Coccolithophore: An Evolutionary Advantage Against Extracellular Oxidative Damage. *Small* **2023**, *19* (44), No. 2300346.
(41) Yang, M.; Batchelor-McAuley, C.; Barton, S.; Rickaby, R. E. M.; Bouman, H. A.; Compton, R. G. Opto-Electrochemical Dissolution Reveals Coccolith Calcium Carbonate Content. *Angew. Chem., Int. Ed.* **2021**, *60* (38), 20999−21006.
(42) Arvidson, R. S.; Collier, M.; Davis, K. J.; Vinson, M. D.; Amonette, J. E.; Luttge, A. Magnesium Inhibition of Calcite Dissolution Kinetics. *Geochim. Cosmochim. Acta* **2006**, *70* (3), 583−594.
(43) Hassenkam, T.; Johnsson, A.; Bechgaard, K.; Stipp, S. L. S. Tracking Single Coccolith Dissolution with Picogram Resolution and Implications for CO_2 Sequestration and Ocean Acidification. *Proc. Natl. Acad. Sci. U.S.A.* **2011**, *108* (21), 8571−8576.
(44) Milner, M. P.; Chen, H.; Yang, J. M.; Compton, R. G. Dissolution Kinetics of Solid Particles and the Role of Aggregation: Vaterite Dissolution. *J. Phys. Chem. C* **2025**, *129* (13), 6316−6321.
(45) Milner, M. P.; Saint, H. A.; Lei, C.; Yang, J. M.; Compton, R. G. Vaterite/Hydroxyapatite Core−Shell Microspheres: Dissolution Kinetics and Mechanism. *J. Phys. Chem. C* **2025**, *129*, 2966−2972.
(46) Streeter, I.; Compton, R. G. Diffusion-Limited Currents to Nanoparticles of Various Shapes Supported on an Electrode; Spheres, Hemispheres, and Distorted Spheres and Hemispheres. *J. Phys. Chem. C* **2007**, *111* (49), 18049−18054.
(47) Compton, R. G.; Banks, C. E. *Understanding Voltammetry*, 4th ed.; World Scientific (Europe), 2025.
(48) Yang, M.; Tan, L.; Batchelor-McAuley, C.; Compton, R. G. The Solubility Product Controls the Rate of Calcite Dissolution in Pure Water and Seawater. *Chem. Sci.* **2024**, *15*, 2464−2472.
(49) Compton, R. G.; Brown, C. A. The Inhibition of Calcite Dissolution/Precipitation: Mg2+ Cations. *J. Colloid Interface Sci.* **1994**, *165* (2), 445−449.
(50) Morton-Collings, T.; Yang, M.; Compton, R. G. Controlling Crystallisation and Dissolution of Biogenic CaCO 3 *via* Dissolved Magnesium Cations. *Environ. Sci.: Adv.* **2024**, *3*, 402−410.
(51) Yang, J. M.; Compton, R. G. The Dissolution and Precipitation Kinetics of Solid Particles: The Influence of Adsorption. *J. Solid State Electrochem.* **2025**, *29* (13), 6316−6321.
(52) Fick, A. Ueber Diffusion. *Ann. Phys.* **1855**, *170* (1), 59−86.
(53) Fick, A. V. On Liquid Diffusion. *London, Edinburgh, Dublin Philos. Mag. J. Sci.* **1855**, *10* (63), 30−39.

https://doi.org/10.1021/acs.jpcc.5c05009
J. Phys. Chem. C 2025, 129, 22334−22341